Boundary layer structure in a rough Rayleigh–Bénard cell filled with air

O. Liot[1], J. Salort[1,†], R. Kaiser[2], R. du Puits[2] and F. Chillà[1]

[1]Laboratoire de physique, UMR CNRS 5672, École Normale Supérieure de Lyon,
46 allée d'Italie, 69364 Lyon CEDEX 7, France

[2]Technische Universität Ilmenau, Institute of Thermodynamics and Fluid Mechanics,
PO Box 100565, 98684 Ilmenau, Germany

In this experimental work, the aim is to understand how turbulent thermal flows are enhanced by the destabilization of the boundary layers. Square-stud roughness elements have been added on the bottom plate of a rectangular Rayleigh–Bénard cell in air, to trigger instabilities in the boundary layers. The top plate is kept smooth. The cell proportions are identical to those of the water cell previously operated and described by Salort *et al.* (*Phys. Fluids*, vol. 26, 2014, 015112), but six times larger. The very large size of the Barrel of Ilmenau allows detailed velocity fields to be obtained using particle image velocimetry very close to the roughness elements. We found that the flow is quite different at low Rayleigh numbers, where there is no heat-transfer enhancement, and at high Rayleigh numbers where there is a heat-transfer enhancement due to the roughness. Below the transition, the fluid inside the notch, i.e. between the studs, is essentially at rest, though it is slowly recirculating. The velocity profiles on the top of obstacles and in grooves are fairly compatible with those obtained in the smooth case. Above the transition, on the other hand, we observe large incursions of the bulk inside the notch, and the velocity profiles on the top of obstacles are closer to the logarithmic profiles expected in the case of turbulent boundary layers.

Key words: turbulent boundary layers, turbulent convection, turbulent flows

1. Introduction

Turbulent thermal convection is an important phenomenon both in nature and in industry. One common model system is the Rayleigh–Bénard cell, which consists in a fluid layer confined inside adiabatic walls, heated from below and cooled from above by horizontal smooth plates. In the limit of Boussinesq conditions, this system is controlled by only three non-dimensional parameters: the Rayleigh number, Ra, the Prandtl number, Pr, and the cell aspect ratio Γ.

† Email address for correspondence: julien.salort@ens-lyon.fr

The Rayleigh number, *Ra*, accounts for the thermal forcing,

$$Ra = \frac{g\alpha(T_h - T_c)H^3}{\nu\kappa}, \tag{1.1}$$

with g the acceleration due to gravity, α the fluid thermal expansion coefficient, T_h the temperature of the hot plate, T_c the temperature of the cold plate, H the cell height, ν the fluid kinematic viscosity and κ the fluid thermal diffusivity.

The Prandtl number, *Pr*, is a property of the fluid and compares the two diffusion mechanisms that impede convection,

$$Pr = \frac{\nu}{\kappa}. \tag{1.2}$$

The aspect ratio, Γ, is a geometric parameter of the cell,

$$\Gamma = \frac{W}{H}, \tag{1.3}$$

where W is the width of the cell and H its height.

The system output can be assessed by the Nusselt number, *Nu*, which compares the thermal heat flux, $\dot{q}$, to the case of a purely diffusive situation where the heat flux, $\dot{q}_{diff}$, is given by

$$\dot{q}_{diff} = \frac{\lambda(T_h - T_c)}{H}, \tag{1.4}$$

where λ is the fluid thermal conductivity. The Nusselt number can thus be written

$$Nu = \frac{\dot{q}H}{\lambda(T_h - T_c)}. \tag{1.5}$$

An important problem is to be able to predict the system heat flux for a given thermal forcing, i.e. to relate the Nusselt number to *Ra* and *Pr*, in particular in the case of asymptotically large forcings. Many scaling theories have been proposed, i.e. expressing the Nusselt numbers as a power law, $Nu = \beta Ra^\gamma$, see reviews by Ahlers, Grossmann & Lohse (2009), Lohse & Xia (2010) and Chillà & Schumacher (2012).

In the turbulent regime, the average temperature within the Rayleigh–Bénard cell is mostly homogeneous, except within thin fluid layers near the plates. Those layers, usually referred to as thermal boundary layers, play an important role in the dynamics of the system. One classical argument consists in considering that the heating and cooling plates are independent, thus the heat flux $\dot{q}$ should not depend on H. This yields $\gamma = 1/3$. This prediction catches the experimental behaviour relatively well, though the situation is more complicated. Many efforts have been made to better model the experimental observations and catch the details of the *Nu* versus *Ra* relation (Castaing *et al.* 1989; Shraiman & Siggia 1990; Grossmann & Lohse 2000; Stevens *et al.* 2013).

In particular, an open problem is the possible destabilization of these boundary layers and its effect on the asymptotic scaling laws. Half a century ago, Kraichnan predicted that the transition to a turbulent boundary layer would increase the scaling law to $\gamma = 1/2$ with logarithmic corrections (Kraichnan 1962). Because this scaling can be derived as a rigorous upper bound (Doering & Constantin 1996), it means that it will not undergo further qualitative changes as *Ra* tends to infinity, and thus this regime is sometimes referred to as the ultimate regime of convection.

There are only a few laboratory set-ups capable of achieving high enough Rayleigh numbers to reach the transition towards this regime. Such an experimental observation was first reported in a cryogenic Rayleigh–Bénard cell using gaseous helium as the working fluid (Chavanne *et al.* 1997). The data are compatible with the prediction from Kraichnan, with logarithmic corrections. The critical Rayleigh number then reported was 10^{11}, though the precise value is somewhat uncertain because it depends on the exponent of the scaling one uses as a reference. A deviation from $Nu \sim Ra^{2/7}$ was considered in the case of the original paper of Chavanne *et al.* If one chooses to consider a deviation from $\gamma = 1/3$ instead, then the same dataset yields a critical Rayleigh number closer to 10^{12}, as was subsequently reported by the Grenoble group (Gauthier *et al.* 2009; Roche *et al.* 2010).

New experimental heat-flux measurements have been reported recently by the MPIDS group in Göttingen for Rayleigh numbers beyond 10^{12}, using pressurized SF_6 as the working fluid (Ahlers *et al.* 2009, 2012*b*; Funfschilling, Bodenschatz & Ahlers 2009; He *et al.* 2012). They have obtained several possible effective scaling exponents, possibly less steep than $\gamma = 1/3$, but eventually close to $\gamma = 0.36$ for $Ra > 10^{14}$. A theoretical interpretation has been proposed by Grossmann & Lohse (2011), based on an extension of their original unifying theory (Grossmann & Lohse 2001) to the case of turbulent boundary layers and logarithmic velocity profiles.

Our alternative approach in the experimental work presented in this paper aims at triggering the transition to a turbulent boundary layer at a lower Rayleigh number by means of a controlled roughness. Indeed, the critical shear Reynolds number can be lowered in the presence of roughness (Schlichting & Gersten 2000).

Several groups have reported roughness-induced heat-transfer enhancements. Groove-shaped roughness has been added to the already-transiting Rayleigh–Bénard cell in Grenoble, which allowed the scaling exponent to be further increased from an effective 0.38 due to the logarithmic corrections to the purely asymptotic $\gamma = 1/2$ (Roche *et al.* 2001). A numerical simulation was performed by Stringano, Pascazio & Verzicco (2006) in this particular geometry and backed the increase of γ.

Pyramid-shaped roughness was used in Hong Kong. Though it does not always produce a change in γ, it still yields enhancement of plume emissions and a 20–76 % increase for *Nu*. This is larger than the increase due to the increase in heating area caused by the roughness (Shen, Tong & Xia 1996; Du & Tong 1998, 2000; Qiu, Xia & Tong 2005). The result has been extended recently to the case where roughness is added on one plate only (Wei *et al.* 2014).

Spherical roughness was used also by Ciliberto & Laroche (1999), distributed either randomly or periodically on the bottom plate. The roughness was made of glass and therefore changed the plate conductivity locally as well. They reported an increase from $\gamma = 2/7$ to a higher exponent, only in the case of randomly distributed spheres.

Our own previous experiment, carried out in Lyon, involved a 40 cm × 40 cm rectangular cell with a rough bottom plate and water as the working fluid (Salort *et al.* 2014). The controlled roughness consisted in an array of obstacles 2 mm high and 5 mm × 5 mm square, evenly spaced every 1 cm. Heat-transfer enhancement was observed and agreed fairly well with measurements with a similar kind of roughness inside a larger cylindrical cell (Tisserand *et al.* 2011).

The careful analysis of the local temperature fluctuations, as well as temperature visualization with background-oriented synthetic schlieren imaging, strongly suggested a destabilization of the laminar boundary layer on the top of the obstacles and a confinement of the flow between the obstacles (referred to as notches). These observations led us to propose a simple model, which accounted for the observed global heat-transfer enhancements (Salort *et al.* 2014).

The roughness-induced heat-transfer enhancement may depend on the details of the roughness geometry, and the influence of the roughness shape may be of great interest for engineers (García *et al.* 2012). However, in this work, we focus on general effects only, obtained once a transition to turbulence inside the boundary layer has been triggered. We choose one particular set of obstacles for its simplicity, and study how the changes in the boundary layer structure affect the dynamics of the heat transport. The aim is to provide experimental evidence of the effects of boundary layer destabilization on the global heat flux. The understanding of the mechanisms at play is of the utmost importance in predicting more generally the heat transfer in the high-Ra limit.

The case of periodic box-shaped roughness elements with spanwise dimension equal to the full depth of the cell has also been studied analytically (Shishkina & Wagner 2011) and numerically (Wagner & Shishkina 2015). The effect of the height, width and distance between the obstacles is studied. They find an increase for γ, which then saturates at larger Ra when the cavities (that we refer to as notches in the present work) are fully washed out. The main differences from the other studies mentioned above are that the height of these roughness elements is much larger than the typical boundary layer thickness, and that the roughness consists only of a set of four obstacles on the plate. Although this might be a different situation than the case considered in the present paper of a rough surface where the roughness has dimensions comparable to those of the boundary layers, and consists of a much larger set of obstacles, it nevertheless triggers changes in the boundary layer structure that can be compared to the situation presented in this work.

In this paper, we present new measurements carried out inside the Barrel of Ilmenau. The Barrel of Ilmenau is the world's largest experiment (up to 7.0 m × 6.3 m) to study highly turbulent convection in air with unrivalled spatial and temporal resolution. A rectangular cell, with proportions strictly identical to the water cell in Lyon, but six times larger, has been inserted inside the Barrel. As in the Lyon experiment, the top plate is smooth and the bottom plate is rough. This configuration has allowed us to study velocity fields using particle image velocimetry (PIV) near the obstacles, as well as the local heat flux on the bottom plate, and thus to go beyond our previous analysis. The observation of logarithmic profiles of velocity reported at high Rayleigh numbers in this work is direct evidence of the destabilization of the boundary layers. This is not to be confused with the logarithmic profiles of temperature that have been observed above smooth plates, in both the classical and ultimate states (Ahlers *et al.* 2012*a*; Ahlers, Bodenschatz & He 2014; Wei & Ahlers 2014), and which do not necessarily imply a transition to turbulent boundary layers.

2. Experimental set-up

The convection cell is a 0.62 m thick, 2.50 m × 2.50 m rectangular cell with 0.50 cm thick walls (see sketch in figure 1). The walls are inserted inside the Barrel of Ilmenau. The bottom and top plates are directly those of the Barrel itself and are described in more detail in previous work by du Puits, Resagk & Thess (2013). The controlled roughness consists in an array of 1.2 cm high, 3 cm × 3 cm square aluminium obstacles, evenly glued on the bottom plate. As shown in figure 2, because these obstacles are aligned with the walls, it is possible to distinguish between 'grooves' washed by the mean wind and 'notches' between obstacles where the fluid is confined.

In this configuration, the rectangular cell is fully surrounded by the larger cylindrical Rayleigh–Bénard cell, 7.15 m in diameter and 2.50 m in height. The vertical
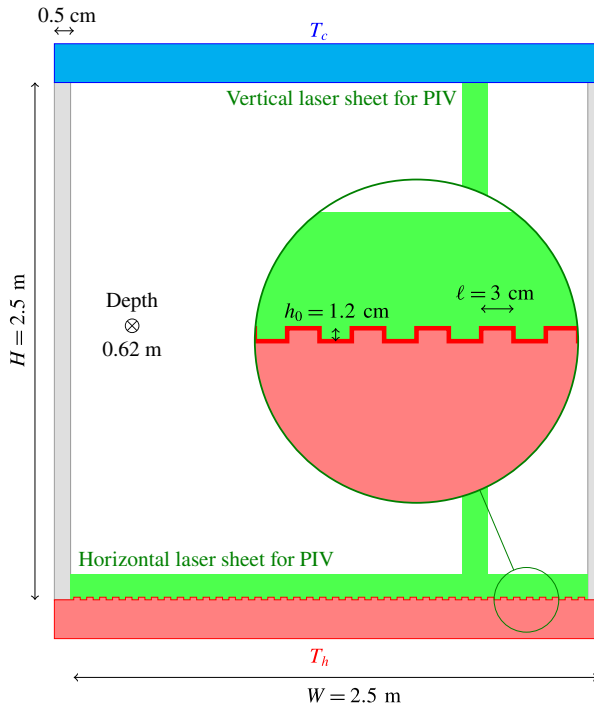
FIGURE 1. (Colour online) Sketch of the convection cell. The green surfaces represent the laser sheets, either vertical for PIV in the groove and on the obstacle, or horizontal for PIV inside the notch.
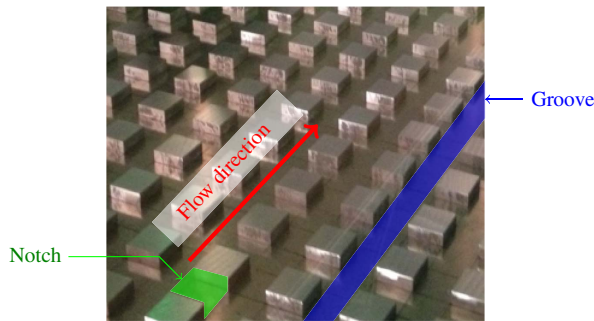

FIGURE 2. (Colour online) Picture of the roughness on the bottom plate. The blue coloured area is an example of a 'groove' portion, washed by the mean wind. The green coloured area is a example of a 'notch', where the fluid is confined between obstacles.

temperature distribution is almost the same inside and outside the enclosure, therefore the lateral heat exchange throughout the walls is negligible. The working fluid is air. The Prandtl number is 0.71.

Although this work is mainly about PIV and characterization of the velocity boundary layers, the Nusselt numbers have also been estimated, to determine when the critical Nusselt number, where roughness-induced heat-transfer enhancement is expected, has been reached. Because there are only three Rayleigh numbers (given in

	T_h (°C)	T_c (°C)	T_m (°C)	P (W)	Ra	Nu
PIV + HFS	23	20	22	200	4.66×10^9	62.1
HFS	25	15	20.9	619	1.59×10^{10}	111
PIV	35	15	27	1700	2.8×10^{10}	
HFS	51.4	21.2	38.1	2090	3.64×10^{10}	247
PIV	55	20	41	4090	4.04×10^{10}	

TABLE 1. Experimental conditions. The first column indicates the kind of measurement that has been performed: particle image velocimetry near the bottom rough plate (PIV) and/or thermal heat-flux measurements (HFS). The Nusselt number is the estimation of the local Nusselt number at $(x, y) = (60, 31$ cm), see text for details.

table 1), it is not possible to infer power-law scalings. The heat flux is computed from three commercial sensors, identical to those used previously in the facility (du Puits, Resagk & Thess 2010; Kaiser & du Puits 2014): two Omega Newport HFS-4 sensors that measure the heat flux on the top of an obstacle, $\dot{q}_{plot}$, and the heat flux inside a notch, $\dot{q}_{notch}$, and one PhyMeas sensor that measures the heat flux in a groove, $\dot{q}_{groove}$.

The radiative heat flux cannot be neglected; it accounts for 10–30 % of the total heat flux in our set-up. To accurately estimate the convective Nusselt number, we subtracted an estimated radiative flux using the same model as Kaiser & du Puits (2014), with emissivities $\epsilon_c = 0.05$ for the cooling plate, $\epsilon_h = 0.07$ for the heating plate and $\epsilon_w = 0.24$ for the walls because they were coated with a thin foil during the heat-flux measurements.

The total convective heat flux, $\dot{q}$, is then estimated by summing the contributions:

$$\dot{q} = \tfrac{1}{2}\dot{q}_{groove} + \tfrac{1}{4}\dot{q}_{notch} + \tfrac{1}{4}\dot{q}_{plot}. \tag{2.1}$$

The three heat-flux sensors are located near one another, close to $x = 60$ cm from the sidewall (horizontal direction in figure 1) and $y = 31$ cm (depth direction in figure 1).

To assess whether there is a heat-transfer enhancement, the Nusselt number obtained from that heat flux is compared in figure 3 with reference data obtained in the same cell but with smooth boundaries. We use previous measurements by Kaiser (2015) as the reference data for the smooth case. Kaiser & du Puits (2014) have shown, however, that the heat flux is not homogeneous on the plate, so comparison between the present local measurement and whole-plate heat fluxes should be carried out with care. Both local and global reference data are available in the smooth case (Kaiser & du Puits 2014). The global values are averages computed from whole-plate heat-flux maps obtained with an infrared camera.

In the present work, we measured local heat fluxes only, and these can be compared to local smooth estimates, computed from the heat-flux map by averaging over a 3 cm × 3 cm area, at the same position as the sensors in the present work on both sides of the cell, because the local heat flux depends on the wind direction.

The transition towards a roughness-induced enhanced heat-transfer regime is expected to occur when the thermal boundary layer thickness, δ_{th}, matches the height of the roughness, h_0 (Tisserand et al. 2011). Therefore, the expected critical Nusselt number, Nu_c, is

$$Nu_c = \frac{H}{2h_0}. \tag{2.2}$$

This critical Nusselt number is shown as a dashed horizontal line in figure 3.
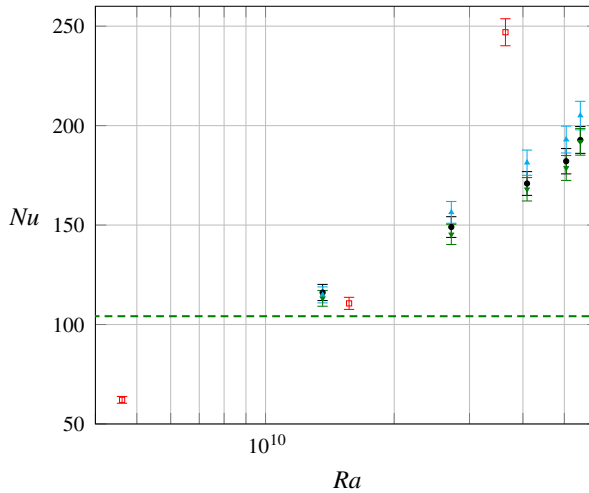
FIGURE 3. (Colour online) Non-dimensional local heat-flux measurements at $x = 60$ cm inside the rough cell (red open squares). The error bars represents the 5.5 % uncertainty of the commercial heat-flux sensors on the dimensionless heat flux. The results from Kaiser (2015) inside a smooth cell are shown for reference: whole-plate heat-flux measurements from an infrared camera (black circles) with an uncertainty of 7 %, with heat flux averaged over a 3 cm × 3 cm area at $x = 60$ cm (down-pointing green triangles) and at $x = 190$ cm (up-pointing cyan triangles). The horizontal dashed line indicates the transition Nusselt number, $Nu_c = H/(2h_0)$, above which a heat-transfer enhancement is expected.

The Nusselt number in the rough case, computed with the local heat flux (2.1), is in quantitative agreement with the smooth case at the intermediate Rayleigh number, $Ra = 1.59 \times 10^{10}$, close to the expected transition threshold. At the lowest Rayleigh number, $Ra = 4.66 \times 10^{9}$, the Nusselt number in the rough case might be slightly lower than expected in the smooth case. This can be caused by the additional heat resistance due to the fluid inside the notch, as was suggested previously by Tisserand *et al.* (2011). The Nusselt number in the rough case at the highest Rayleigh number, $Ra = 3.64 \times 10^{10}$, is higher than the Nusselt number in the smooth case. This can be interpreted as roughness-triggered heat-transfer enhancement.

2.1. *Velocity measurements*

The flow was seeded with cold-atomized droplets of di-ethyl-hexyl-sebacate with a typical size of 1 µm, identical to those used previously by du Puits *et al.* (2014). Their size is sufficiently small for them to behave as tracers. As shown in figure 1, these particles were illuminated with either a horizontal (for visualization in the groove and on the top of the obstacles) or vertical (for visualization inside the notch) laser light sheet of about 70 mm height and 2 mm thickness, generated by a 2 W cw laser in combination with a beam expander. The fast acquisition of the particle motion was captured using an IOI Flare-2M360-CL 2048 × 1088 camera with a frame rate between 340 Hz at the lowest Ra at full resolution and 902.5 Hz at the highest Ra at 2040 × 400 resolution.

We have recorded three sequences of 20 s every five minutes at the lowest Ra, or every minute at the highest Ra, and sequences of 2 s every minute for one hour at all Ra. The velocity fields are then computed using a cross-correlation PIV algorithm

Streamwise velocity (along x)	$u(x, z, t)$
Streamwise velocity fluctuation	$u' = u(x, z, t) - \langle u(x, z, t) \rangle_t$
Plate-normal velocity (along z)	$v(x, z, t)$
Plate-normal velocity fluctuation	$v' = v(x, z, t) - \langle v(x, z, t) \rangle_t$
Boundary layer thickness (crossing of tangent with u_{max})	$\delta_\times$
Displacement thickness	$\delta_{thickness}$
Distance to the wall where $u = u_{max}$	δ_{max}
Viscous sublayer thickness	δ
Thermal boundary layer thickness	δ_{th}
Shear Reynolds number	$Re_s = \delta_{thickness} u_{max}/\nu$
Shear stress	$\tau = \langle u'v' \rangle_t + \mu(\partial u/\partial z)$
Typical turbulent velocity	$U^* = \sqrt{\langle u'v' \rangle_t}$
Non-dimensional wall distance	$z^+ = z U^*/\nu$
Non-dimensional velocity	$u^+ = u/U^*$
Height of the cell	$H = 2.5$ m
Depth of the cell (spanwise)	0.62 m
Height of roughness elements	$h_0 = 1.2$ cm
Width of roughness elements	$\ell = 3.0$ cm

TABLE 2. Summary of the notations and main dimensions of the system.

implemented in the CIVx software suite (Fincham & Delerce 2000), above and below the critical Nusselt number Nu_c, and near several positions on the rough plate: on top of an obstacle, in a groove and inside a notch (see figure 4).

The fluid inside the notch is almost at rest, as indirectly assumed by Salort *et al.* (2014). Due to the limitations of our acquisition system, it is not possible to resolve the details of both the slow recirculation inside the notch and the much faster flow away from the plate. That is why we used separate acquisitions: acquisitions above the obstacle (figure 4a,b) and measurements inside the notch only (figure 4c,d).

2.2. *Notations for the similarity parameters*

Our aim is to compare the flow features, in particular the velocity profiles, velocity boundary layer thickness and the turbulent fluctuations, above and below Nu_c, and compare them with smooth experimental data from the literature, and with simple classical theoretical profiles, such as the Prandtl–Blasius viscous velocity profile or the logarithmic velocity profile of isothermal turbulent shear flows (Schlichting & Gersten 2000).

In order to perform such kinds of comparison, it is necessary to specify the non-dimensional parameters and the definition of the boundary layer thickness. The notations that we use in our analysis are summarized in table 2.

As pointed out by previous experimental investigations of the velocity profiles, such as du Puits, Resagk & Thess (2007), the comparison with Blasius would normally require computation of the similarity parameter $\eta = z\sqrt{u_{max}/\nu x}$, and one possibility would be to follow the implicit assumption of Grossmann & Lohse (2000) that the development of the boundary layer starts at the outer edge of the plate. But then the experimental profiles drastically differ from the Blasius profile, and this observation holds also for the data reported in this paper. The comparison with Blasius-type profiles seems possible, however, if x is specified in such a way that the velocity

gradients du/dz of the Blasius prediction and the experimental data are made to match, or equivalently if the profiles are plotted in terms of $z/\delta_{\times}$ where $\delta_{\times}$ is obtained as the distance from the plate at which the extrapolation of the tangent at $z = 0$ crosses u_{max} (Sun, Cheung & Xia 2008; Zhou & Xia 2010).

However, $du/dz|_{z=0}$ is ill-defined for some of the profiles above Nu_c. This will be discussed in more detail in the following sections. For this reason, and also to allow comparison of the shear Reynolds number measured in the smooth case by Li *et al.* (2012) and Willert, du Puits & Resagk (2014), it is useful to use the displacement thickness $\delta_{displacement}$ as an alternative definition of the boundary layer thickness,

$$\delta_{displacement}(x) = \int_0^\infty \left(1 - \frac{\langle u(x, z, t)\rangle_t}{u_{max}} \right) dz, \qquad (2.3)$$

where $\langle\cdot\rangle_t$ is the temporal average. In practice, the upper bound is chosen at the distance δ_{max} where $u(z_{max}) = u_{max}$.

The comparison with logarithmic profiles of classical turbulent shear flows requires one to define $z^+ = zU^*/\nu$ and $u^+ = u/U^*$, where U^* is a characteristic velocity of the turbulent flow considered, defined such that

$$\tau = \rho U^{*2}, \qquad (2.4)$$

where τ is the shear stress (Landau & Lifshitz 1987). This shear stress is linked to the Reynolds tensor and the velocity gradient:

$$\tau = \rho \langle u'v'\rangle_t + \mu \frac{\partial u}{\partial z}, \qquad (2.5)$$

where $\mu = \nu\rho$ is the dynamic viscosity of the fluid.

In experimental works where the velocity gradient is well defined and well resolved at $z = 0$, such as du Puits *et al.* (2007) and Willert *et al.* (2014), the shear stress can be computed at the wall, e.g. $\tau_w = \mu\partial u/\partial z$. In the following, we will rather compute τ away from the plate, where the velocity gradient is negligible, i.e. $\tau_{turb} = \rho\langle u'v'\rangle$, and therefore

$$U^* = \sqrt{\langle u'v'\rangle_t}. \qquad (2.6)$$

3. The flow field adjacent to the roughness elements

3.1. *The flow field below and beyond the transition limit*

There are three main simple flow structures that can be considered inside the notch, between roughness elements, sketched in figure 5: (*a*) stratified fluid inside the notch, below the critical limit of linear instability, with no velocity. This would lead to reduced heat transfer compared to the case of the smooth plate, as was observed by Tisserand *et al.* (2011) in a cylindrical cell; (*b*) slow circulation inside the notch with no fluid exchange, caused by internal convection and shear from the wind. In that case, there is only weak additional thermal resistance and the boundary condition at $z = h_0$ is almost unchanged, compared to the top of the obstacle; (*c*) convection and mixing with the bulk flow. In that case, the notch may contribute to the heat-transfer enhancement or to the plume emission.

The experimental velocity fields are shown in figure 4 and provide evidence of a change of flow structure inside the notch from configuration (*b*) at $Ra = 4.66 \times 10^9$ to configuration (*c*) at $Ra = 4.04 \times 10^{10}$. This change occurs concomitantly with heat-transfer enhancement and changes in the velocity statistics that we detail in the following subsections.
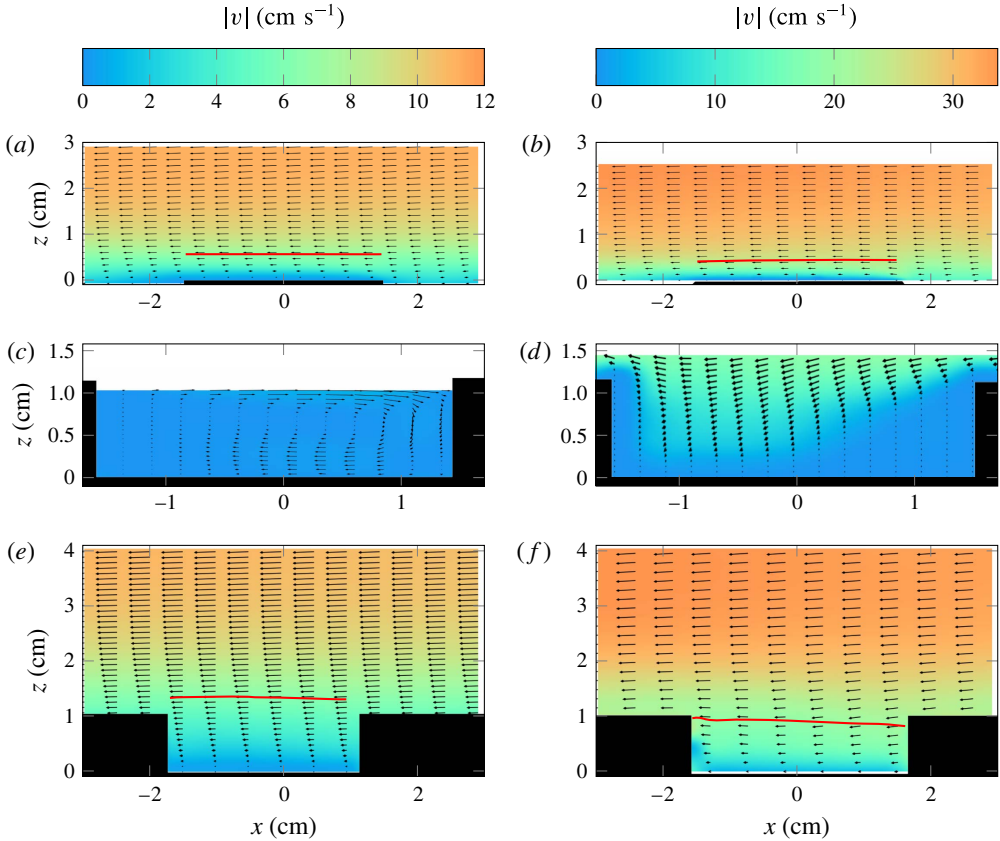
FIGURE 4. (Colour online) Mean velocity fields at $Ra = 4.66 \times 10^9$ (a,c,e) and $Ra = 4.04 \times 10^{10}$ (b,d,f). (a,b) On top of an obstacle, (c,d) inside a notch, (e,f) in a groove. The colour code is given for one Rayleigh number and is identical for the three locations. The scale of the arrows is arbitrary and differs from one plot to another to allow better visualization of the flow. The solid red line is the velocity displacement thickness, $\delta_{displacement}$ (see (2.3)).
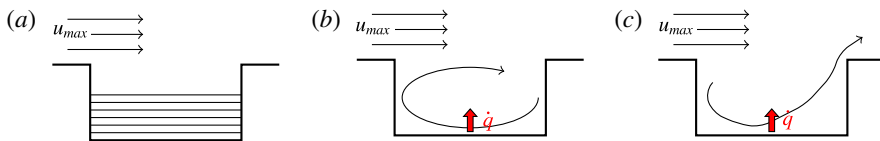

FIGURE 5. (Colour online) Sketch of possible flow structure inside a notch. (a) Thermally stratified, no convection, (b) internal convection, no fluid exchange, (c) external convection with fluid exchange.

3.2. *Flow structure below the transition*

The velocity profiles below the transition Nusselt number Nu_c are shown in figure 6. They compare fairly well with typical profiles previously obtained in smooth cells (du Puits *et al.* 2007; Sun *et al.* 2008; Li *et al.* 2012). The negative mean velocities for $z < 0.5$ cm inside the notch are a signature of the slow recirculation. The measurements collapse quickly above the obstacles.
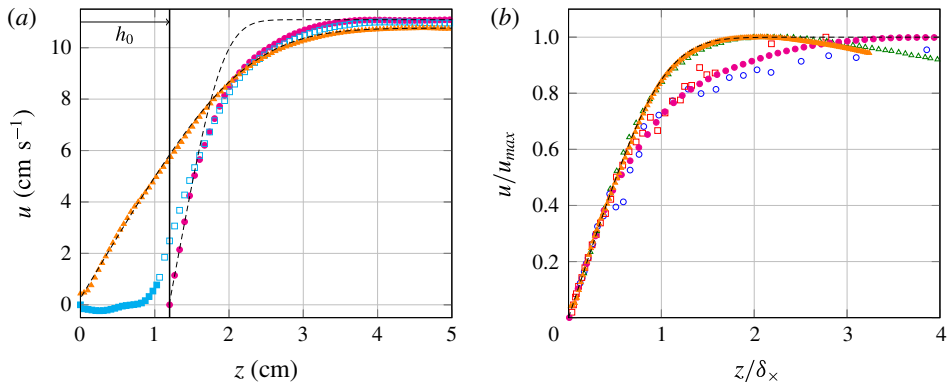
FIGURE 6. (Colour online) Velocity profiles near the rough plate at $Ra = 4.66 \times 10^9$, in a groove (full orange triangles), on the top of a roughness element (full magenta circles) and inside a notch (cyan squares, full symbols obtained with the acquisition inside the notch, open symbols with the acquisition above the notch, away from the plate). The black dashed lines are the theoretical Prandtl–Blasius profiles. (*a*) Raw profiles where the origin $z = 0$ is the bottom of the roughness elements. (*b*) Non-dimensional profiles compared with experimental data obtained in smooth cells at $Ra = 7.48 \times 10^{11}$ from du Puits *et al.* (2007) (open blue circles), at $Ra = 3 \times 10^9$ from Li *et al.* (2012) (open red squares) and at $Ra = 5.3 \times 10^9$ from Sun *et al.* (2008) (open green triangles).

The profiles above an obstacle or above a notch are very similar for $z > h_0$. The reason is that the boundary condition is close: zero velocity at $z = h_0$ above obstacles, or almost zero velocity at $z = h_0$ above notches. In other words, above obstacles and notches the velocity goes from 0 at $z = h_0$ to u_{max} at $z = \delta_{max}$, and in the groove it goes from 0 at $z = 0$ to u_{max} at a nearly similar $z = \delta_{max}$. For this reason, the profile is much steeper above notches and obstacles than in the groove, and thus $\delta_\times$, defined from the slope at origin, is much smaller in the former case.

Once shifted in z (by choosing $z = 0$ on the top of the obstacle, rather than at the bottom of the obstacle for the profiles above the notch and above the roughness element) and rescaled by $\delta_\times$, the tangents at the origin are indeed collapsed, and the shape of the profile can be compared to other profiles found in the literature, and to theoretical velocity profiles (figure 6*b*). The profile above a roughness element differs slightly from the Prandtl–Blasius profile, and is consistent with the results from du Puits *et al.* (2007) and Li *et al.* (2012) obtained in the Barrel with smooth plates. On the other hand, the profiles in a groove are much closer to the profiles obtained by Sun *et al.* (2008) and to the laminar Prandtl–Blasius profile. This may be a consequence of the confinement and the additional drag caused by the rough walls, which yields locally a smaller Reynolds number.

The displacement thickness, plotted in figure 4, is larger than h_0. At the lowest Rayleigh number, $Ra = 4.66 \times 10^9$, we find $\delta_{displacement} = 1.4$ cm in the groove, or 0.7 cm and 0.56 cm beyond $z = h_0$, respectively above the notch and above the roughness element. Hence, the thickness of the boundary layer, δ_v, defined from $z = 0$ at the bottom of roughness elements, lies between 1.4 and 1.9 cm. To compare these observations to previous results, one has to infer an estimate for the thermal boundary layer thickness. Since the Prandtl number is less than 1, the thermal boundary layer is thicker than the kinetic boundary layer. For Prandtl–Blasius boundary layers, one can show that δ_{th}/δ_v scales like $\sim Pr^{-1/3}$ for large Prandtl numbers and like $\sim Pr^{-1/2}$ for
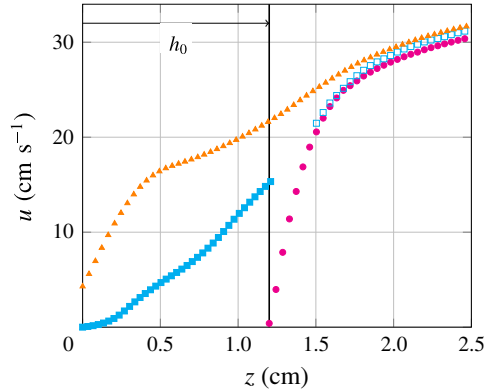
FIGURE 7. (Colour online) Velocity profiles near the rough plate at $Ra = 4.04 \times 10^{10}$, in a groove (full orange triangles), on the top of a roughness element (full magenta circles) and inside a notch (full cyan squares: acquisition of the low velocities, open cyan squares: acquisition of the fast velocities).

small Prandtl numbers (Shishkina, Horn & Wagner 2013). In the range of intermediate Prandtl numbers where the present experiment lies, close to the centre of the cell, the direct numerical simulation study by Shishkina *et al.* (2013) yields

$$\delta_{th} \approx 2.0 \; \delta_v. \tag{3.1}$$

Therefore, the thermal boundary layer thickness can be estimated to lie in the range between 2.8 and 3.8 cm, which is indeed larger than h_0, as expected.

The outer velocity is $u_{max} = 11$ cm s^{-1}. Thus, the shear Reynolds number,

$$Re_s = \frac{\delta_v u_{max}}{\nu}, \tag{3.2}$$

is of order 100. This is consistent with the measurements in the same conditions but over smooth surfaces (Willert *et al.* 2014).

3.3. *Flow structure beyond the transition*

At high Rayleigh number, the flow structure changes substantially: (i) the notches are fully washed by the mean flow and exchange fluid with the turbulent bulk, (ii) the velocity profile features are very different both quantitatively and qualitatively and (iii) the velocity fluctuations are relatively higher. The profiles substantially differ as well from those obtained at lower Rayleigh number: there are inflection points and changes of slope, and there is no horizontal asymptote (see figure 7). The inflection points and changes of slope for $z < h_0$ may be a consequence of the drag on the rough walls. For these reasons, these data do not allow us to compute an accurate estimate for the velocity boundary layer. $\delta_\times$ is ill-defined because it is not clear how to define $\partial u / \partial z$ at $z = 0$ with these profiles; $\delta_{displacement}$ can be estimated by integrating as far away from the plate as possible, yielding possibly biased values (e.g. possibly undervalued). Yet, we find $\delta_{displacement} = 0.90$ cm smaller indeed than h_0 in the groove, and $\delta_{displacement} = 0.47$ cm on the top of the obstacle.

It is not possible to find the maximum velocity u_{max}. The typical value of the wind, however, appears to be only 3–4 times larger than before the transition, while
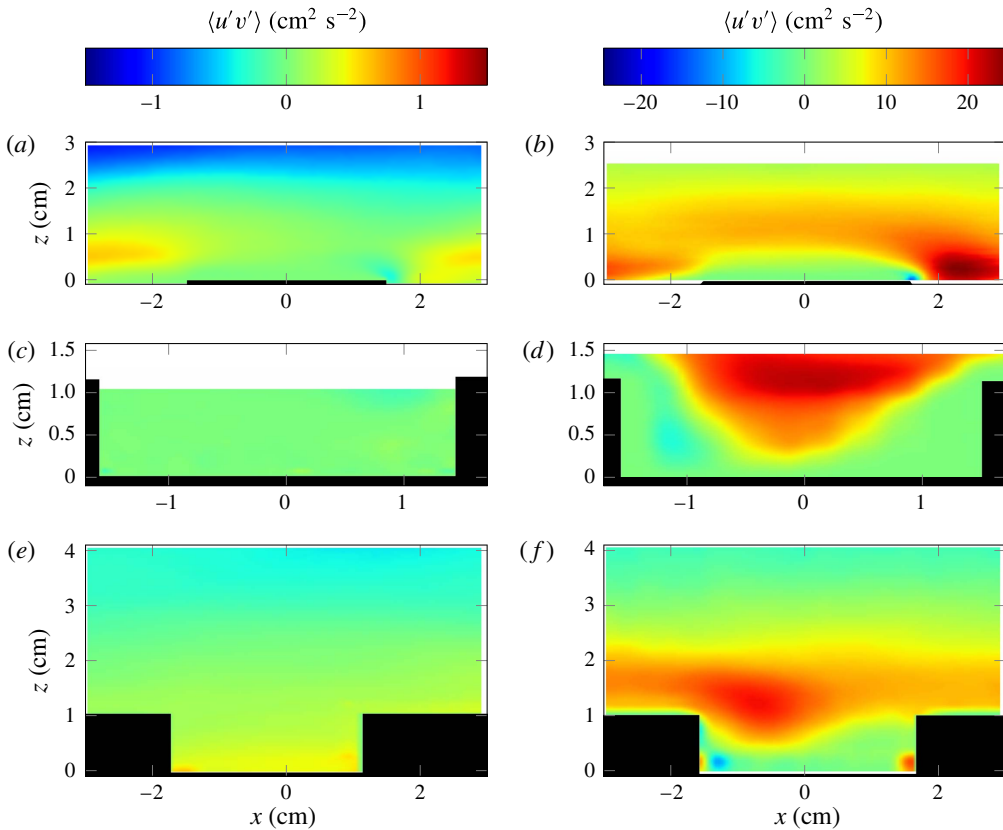
FIGURE 8. (Colour online) Reynolds tensor at $Ra = 4.66 \times 10^9$ (a,c,e) and $Ra = 4.04 \times 10^{10}$ (b,d,f). (a,b) On top of an obstacle, (c,d) inside a notch, (e,f) in a groove. The colour code is given for one Rayleigh number and is identical for the three locations. (a,c,e) Yields $U^\star = 0.77$ cm s^{-1} at $Ra = 4.66 \times 10^9$, (b,d,f) $U^\star = 4.96$ cm s^{-1} at $Ra = 4.04 \times 10^{10}$.

the Reynolds tensor $\langle u'v' \rangle$, on the other hand, is typically 50 times larger after the transition. The fields of $\langle u'v' \rangle$ are given in figure 8. The maximum value of the Reynolds tensor can be used as a definition for $U^\star$. We find $U^\star = 4.96$ cm s^{-1} at $Ra = 4.04 \times 10^{10}$, which allows us to compute the typical scale $z^\star$, defined as

$$z^\star = \frac{\nu}{U^\star}, \tag{3.3}$$

and an estimate of the thickness of the viscous sublayer, δ, classically defined as (Tennekes & Lumley 1987)

$$\delta \approx 5z^\star. \tag{3.4}$$

This yields $\delta \approx 1.7$ mm.

The figure shows, after the transition, regions with high values of $\langle u'v' \rangle$, particularly downstream obstacles, yielding regions of high strain near the top of the obstacles. This suggests a possible transition to a turbulent boundary layer, specifically on the top of the obstacles, in agreement with our previous indirect observations in water (Salort *et al.* 2014). These regions can be seen also in the groove, further downstream
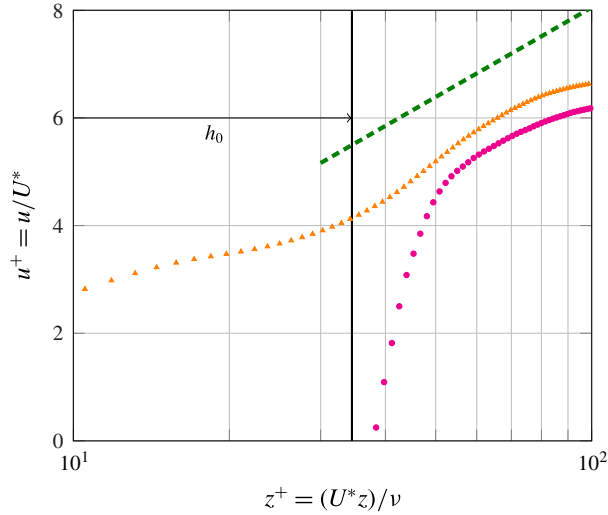
FIGURE 9. (Colour online) Non-dimensional velocity profile in a groove (orange triangles) and above an obstacle (magenta circles) at $Ra = 4.04 \times 10^{10}$. Green dashed line: $2.40 \log z^+ + B$.

than those inside the notch. These regions may be interpreted as wakes produced by the obstacles, advected streamwise, as well as spanwise, downstream of the roughness elements. One may note that the typical turbulent velocity, U^*, associated with those structures is found to be nearly identical in the three fields.

To figure out whether these turbulent wakes can trigger a transition towards a turbulent boundary layer on the top of obstacles, the velocity profiles are compared in figure 9 to the classical prediction for $z^+ > 30$, where one expects logarithmic velocity profiles (Tennekes & Lumley 1987),

$$u = U^\star(2.40 \log z^+ + B), \tag{3.5}$$

where $z^+ = z/z^\star$ and $B = 5.84$ over a smooth surface. The surface can be considered rough when the viscous sublayer is thinner than the typical roughness size. This is indeed the case here since the estimate for the viscous sublayer is 1.7 mm, much smaller than $h_0 = 1.2$ cm. Thus, B is expected to be a function of k^+,

$$k^+ = \frac{h_0}{\delta} = \frac{h_0 U^*}{\nu}. \tag{3.6}$$

In the present measurements, k^+ is of order 40 and lies in the range of the 'transition' regime. The fully rough regime is usually expected for $k^+ \gg 100$ (Tennekes & Lumley 1987; Schlichting & Gersten 2000). In this transition regime, however, B is known to be between -5 and 5, at least in the classical case of sand roughness, but the exact value may differ in the present case of square roughness. The green dashed line in figure 9 is plotted with $B = -3$. In the range of scales that we could measure, the experimental data thus appear to be compatible with such a logarithmic profile.

In addition to this destabilization of the boundary layer on top of obstacles, the mean velocity fields in figure 4 show that, while the flow above the notch is mostly unaffected and is nearly horizontal at the lowest Rayleigh number, it gets a vertical

component after the transition which allows for matter transfers between the bulk and the notch. Evidence for effects of this kind has also been found in other experimental systems (Du & Tong 2000), and they are associated with an increase in the thermal transport without change of the scaling law.

3.4. *Comparison with thermal boundary layer measurements*

Our results should be compared to those obtained from temperature measurements in water, and to what could be expected if the interpretation of the transition features observed in similar conditions in the water cell does hold. In the previous water experiment in Lyon (Salort *et al.* 2014), which was six times smaller, we measured the thermal boundary layer thickness directly from the mean temperature profiles. The result was that

$$\delta_{th,water} \lesssim 0.4 \text{ mm}, \tag{3.7}$$

much thinner than the classical laminar predictions or similar experimental measurements over smooth surfaces. This was one of the arguments for proposing a model based on the roughness-triggered destabilization of the boundary layers.

The mechanisms at play in the present situation in air are expected to be similar. Of course, it is possible that the details of the boundary layer structure differ in these two situations because of the Prandtl number ($Pr = 0.71$ in the present experiment; Pr between 4 and 8 in the water experiment). Yet, both Prandtl numbers are of order 1, and the typical orders of magnitude should agree if the relevant mechanism is similar.

One way to carry out such a comparison is to infer an estimate for the thermal boundary layer thickness from the present velocity boundary layer measurements. The mean velocity boundary layer observed near the rough plate in the present PIV fields can be interpreted in terms of a turbulent boundary layer and viscous sublayer. Because of the efficient mixing in the turbulent boundary layer, one may assume that most of the temperature drop occurs inside the viscous sublayer. Since the Prandtl number is less than 1, the thermal boundary layer is thicker than the kinetic viscous sublayer. The analytical and numerical study by Shishkina *et al.* (2013) shows that the ratio of the thermal and kinetic boundary layer thicknesses depends greatly on the angle β at which the wind attacks the plate. It is not clear how to extrapolate results obtained in the laminar case to the present situation with turbulent boundary layers. Therefore, the following discussion should be understood in terms of orders of magnitude only. For $Pr = 0.786$, in the case of a laminar boundary layer, Shishkina *et al.* (2013) find δ_{th}/δ_v in the range between 1.08 (for $\beta = \pi$) and 2.37 (for $\beta = \pi/2$). The flow in the logarithmic layer above the viscous sublayer is turbulent and does not yield a constant and homogeneous value for β, thus we may only assume that

$$1.08\delta < \delta_{th} < 2.37\delta, \tag{3.8}$$

i.e.,

$$1.8 \text{ mm} < \delta_{th} < 4.0 \text{ mm}. \tag{3.9}$$

Considering that (1) the thermal boundary layer can be written in terms of the Nusselt number,

$$\delta_{th} = \frac{H}{2Nu}, \tag{3.10}$$

and (2) the Nusselt number is a function of Ra and Pr only, then δ_{th} is expected to be proportional to the cell height H if the Rayleigh numbers and all the other control

parameters are equal, hence allowing a comparison of the results: the estimates of δ_{th} are expected to lie within the same ratios with respect to the cell heights.

We previously showed $\delta_{th,water} \lesssim 0.4$ mm in the water experiment at similar Nusselt number (Salort *et al.* 2014); we thus expect $\delta_{th} \lesssim 2.4$ mm in the present set-up in air with dimensions six times larger. The present estimated range for δ_{th}, inferred from the velocity measurements (3.9), is indeed compatible with that prediction.

4. Conclusions

Highly resolved PIV measurements have been undertaken in turbulent Rayleigh–Bénard convection in air with a rough surface of the heating plate. A particular feature of convection at a rough surface is the transition in the scaling of the heat transfer beyond a critical Rayleigh number. Our measurements demonstrate that this transition can be associated clearly with a transition of the flow field around and in between the obstacles.

The interpretation of our previous experimental measurements in water and the phenomenological model derived from them made several implicit assumptions that have been verified in a much more direct fashion in the present work in air. An important assumption was that the flow structure below the roughness-induced transition was identical to the smooth case. The present analysis of the velocity features at $Ra = 4.66 \times 10^9$ backs up this hypothesis: the velocity profiles are fairly similar to those obtained in smooth cells, and they are identical above obstacles, notches or grooves, a fraction of h_0 away from the plate. For Rayleigh numbers lower than the transition value, this work shows indeed that the statistical quantities of the flow, e.g. Reynolds number, mean velocity profile and the mean velocity field, are impacted by the roughness elements only very close to the plate. In all respects, the flow is fairly similar to the smooth case.

There was also indirect evidence in the water experiment, above the critical roughness-induced Rayleigh number, that the boundary layer on the top of the obstacle was no longer laminar. In the present work, we have sought direct evidence of a possible transition to a turbulent boundary layer by means of high-resolution PIV measurements near the roughness elements. We find a high value for the Reynolds tensor $\langle u'v' \rangle$, in quantitative agreement with the expectations in terms of inferred viscous sublayer thickness.

The observations allowed us to go into more detail than the temperature-based analysis in water: we found evidence for both turbulent structures in the wakes of the roughness elements and incursions of the bulk between the obstacles. This leads to a change in the velocity statistics near the plate. In particular, the velocity profiles differ dramatically from the typical profiles obtained in the smooth case.

The incursions in the bulk are still fairly moderate. An important perspective would be to go further, in terms of Nu/Nu_c, and find out how the flow structure is modified when the notches are much more fully washed. Recent simulations by Wagner & Shishkina (2015) suggest that the roughness-induced heat-flux enhancement would then saturate, with a power-law exponent back to 1/3. This could be done in the future with the use of elements of higher roughness.

Acknowledgements

REFERENCES

AHLERS, G., BODENSCHATZ, E., FUNFSCHILLING, D., GROSSMANN, S., HE, X., LOHSE, D., STEVENS, R. J. A. M. & VERZICCO, R. 2012*a* Logarithmic temperature profiles in turbulent Rayleigh–Bénard convection. *Phys. Rev. Lett.* **109**, 114501.

AHLERS, G., BODENSCHATZ, E. & HE, X. 2014 Logarithmic temperature profiles in turbulent Rayleigh-Bénard convection in the classical and ultimate state for a Prandtl number of 0.8. *J. Fluid Mech.* **758**, 436–467.

AHLERS, G., GROSSMANN, S. & LOHSE, D. 2009 Heat transfer and large scale dynamics in turbulent Rayleigh-Bénard convection. *Rev. Mod. Phys.* **81**, 503–537.

AHLERS, G., HE, X., FUNFSCHILLING, D. & BODENSCHATZ, E. 2012*b* Heat transport by turbulent Rayleigh-Bénard convection for $Pr \simeq 0.8$ and $3 \times 10^{12} < Ra < 10^{15}$: aspect ratio $\Gamma = 0.50$. *New J. Phys.* **14**, 103012.

CASTAING, B., GUNARATNE, G., HESLOT, F., KADANOFF, L., LIBCHABER, A., THOMAE, S., WU, X., ZALESKI, S. & ZANETTI, G. 1989 Scaling of hard thermal turbulence in Rayleigh–Bénard convection. *J. Fluid Mech.* **204**, 1–30.

CHAVANNE, X., CHILLÀ, F., CASTAING, B., HÉBRAL, B., CHABAUD, B. & CHAUSSY, J. 1997 Observation of the ultimate regime in Rayleigh–Bénard convection. *Phys. Rev. Lett.* **79**, 3648–3651.

CHILLÀ, F. & SCHUMACHER, J. 2012 New perspectives in turbulent Rayleigh–Bénard convection. *Eur. Phys. J.* E **35**, 58.

CILIBERTO, S. & LAROCHE, C. 1999 Random roughness of boundary increases the turbulent convection scaling exponent. *Phys. Rev. Lett.* **82** (20), 3998.

DOERING, C. R. & CONSTANTIN, P. 1996 Variational bounds on energy dissipation in incompressible flows. III. Convection. *Phys. Rev.* E **53** (6), 5957.

DU, Y.-B. & TONG, P. 1998 Enhanced heat transport in turbulent convection over a rough surface. *Phys. Rev. Lett.* **81** (5), 987–990.

DU, Y.-B. & TONG, P. 2000 Turbulent thermal convection in a cell with ordered rough boundaries. *J. Fluid Mech.* **407**, 57–84.

FINCHAM, A. & DELERCE, G. 2000 Advanced optimization of correlation imaging velocimetry algorithms. *Exp. Fluids Suppl.* **29**, S13–S22.

FUNFSCHILLING, D., BODENSCHATZ, E. & AHLERS, G. 2009 Search for the 'Ultimate State' in turbulent Rayleigh–Bénard convection. *Phys. Rev. Lett.* **103**, 014503.

GARCÍA, A., SOLANO, J. P., VICENTE, P. G. & VIEDMA, A. 2012 The influence of artificial roughness shape on heat transfer enhancement: corrugated tubes, dimpled tubes and wire coils. *Appl. Therm. Engng.* **35**, 196–201.

GAUTHIER, F., SALORT, J., BOURGEOIS, O., GARDEN, J.-L., DU PUITS, R., THESS, A. & ROCHE, P.-E. 2009 Transition on local temperature fluctuations in highly turbulent convection. *Europhys. Lett.* **87**, 44006.

GROSSMANN, S. & LOHSE, D. 2000 Scaling in thermal convection: a unifying theory. *J. Fluid Mech.* **407**, 27–56.

GROSSMANN, S. & LOHSE, D. 2001 Thermal convection for large Prandtl numbers. *Phys. Rev. Lett.* **86** (15), 3316–3319.

GROSSMANN, S. & LOHSE, D. 2011 Multiple scaling in the ultimate regime of thermal convection. *Phys. Fluids* **23**, 045108.

HE, X., FUNFSCHILLING, D., NOBACH, H., BODENSCHATZ, E. & AHLERS, G. 2012 Transition to the ultimate state of turbulent Rayleigh–Bénard convection. *Phys. Rev. Lett.* **108**, 024502.

KAISER, R. 2015 Wärmestromverteilung in turbulenter Rayleigh–Bénard–Konvektion. PhD thesis, Technische Universität Ilmenau.

KAISER, R. & DU PUITS, R. 2014 Local wall heat flux in confined thermal convection. *Intl. J. Heat Mass Transfer* **73**, 752–760.

KRAICHNAN, R. H. 1962 Turbulent thermal convection at arbitrary Prandtl number. *Phys. Fluids* **5** (11), 1374–1389.

LANDAU, L. D. & LIFSHITZ, E. M. 1987 *Fluid Mechanics*, 2nd edn. Course of Theoretical Physics, vol. 6. Butterworth-Heinemann.

LI, L., SHI, N., DU PUITS, R., RESAGK, C., SCHUMACHER, J. & THESS, A. 2012 Boundary layer analysis in turbulent Rayleigh–Bénard convection in air: experiment versus simulation. *Phys. Rev. E* **86**, 026315.

LOHSE, D. & XIA, K.-Q. 2010 Small-scale properties of turbulent Rayleigh–Bénard convection. *Annu. Rev. Fluid Mech.* **42**, 335–364.

DU PUITS, R., LI, L., RESAGK, C. & THESS, A. 2014 Turbulent boundary layer in high Rayleigh number convection in air. *Phys. Rev. Lett.* **112**, 124301.

DU PUITS, R., RESAGK, C. & THESS, A. 2007 Mean velocity profile in confined turbulent convection. *Phys. Rev. Lett.* **99**, 234504.

DU PUITS, R., RESAGK, C. & THESS, A. 2010 Measurements of the instantaneous local heat flux in turbulent Rayleigh-Bénard convection. *New J. Phys.* **12**, 075023.

DU PUITS, R., RESAGK, C. & THESS, A. 2013 Thermal boundary layers in turbulent Rayleigh–Bénard convection at aspect ratios between 1 and 9. *New J. Phys.* **15**, 013040.

QIU, X.-L., XIA, K.-Q. & TONG, P. 2005 Experimental study of velocity boundary layer near a rough conducting surface in turbulent natural convection. *J. Turbul.* **6** (30), 1–13.

ROCHE, P.-E., CASTAING, B., CHABAUD, B. & HÉBRAL, B. 2001 Observation of the 1/2 power law in Rayleigh–Bénard convection. *Phys. Rev. E* **63**, 045303(R)1–4.

ROCHE, P.-E., GAUTHIER, F., KAISER, R. & SALORT, J. 2010 On the triggering of the ultimate regime of convection. *New J. Phys.* **12**, 085014.

SALORT, J., LIOT, O., RUSAOUEN, E., SEYCHELLES, F., TISSERAND, J.-C., CREYSSELS, M., CASTAING, B. & CHILLÀ, F. 2014 Thermal boundary layer near roughnesses in turbulent Rayleigh–Bénard convection: flow structure and multistability. *Phys. Fluids* **26**, 015112.

SCHLICHTING, H. & GERSTEN, K. 2000 *Boundary-Layer Theory*, 8th edn. Springer.

SHEN, Y., TONG, P. & XIA, K.-Q. 1996 Turbulent convection over rough surfaces. *Phys. Rev. Lett.* **76** (6), 908.

SHISHKINA, O., HORN, S. & WAGNER, S. 2013 Falkner–Skan boundary layer approximation in Rayleigh–Bénard convection. *J. Fluid Mech.* **730**, 442–463.

SHISHKINA, O. & WAGNER, C. 2011 Modelling the influence of wall roughness on heat transfer in thermal convection. *J. Fluid Mech.* **686**, 568–582.

SHRAIMAN, B. I. & SIGGIA, E. D. 1990 Heat transport in high-Rayleigh-number convection. *Phys. Rev. A* **42** (6), 3650–3653.

STEVENS, R. J. A. M., VAN DER POEL, E. P., GROSSMANN, S. & LOHSE, D. 2013 The unifying theory of scaling in thermal convection: the updated prefactors. *J. Fluid Mech.* **730**, 295–308.

STRINGANO, G., PASCAZIO, G. & VERZICCO, R. 2006 Turbulent thermal convection over grooved plates. *J. Fluid Mech.* **557**, 307–336.

SUN, C., CHEUNG, Y.-H. & XIA, K.-Q. 2008 Experimental studies of the viscous boundary layer properties in turbulent Rayleigh–Bénard convection. *J. Fluid Mech.* **605**, 79–113.

TENNEKES, H. & LUMLEY, J. L. 1987 *A First Course in Turbulence*. MIT Press.

TISSERAND, J.-C., CREYSSELS, M., GASTEUIL, Y., PABIOU, H., GIBERT, M., CASTAING, B. & CHILLÀ, F. 2011 Comparison between rough and smooth plates within the same Rayleigh–Bénard cell. *Phys. Fluids* **23**, 015105.

WAGNER, S. & SHISHKINA, O. 2015 Heat flux enhancement by regular surface roughness in turbulent thermal convection. *J. Fluid Mech.* **763**, 109–135.

WEI, P. & AHLERS, G. 2014 Logarithmic temperature profiles in the bulk of turbulent Rayleigh–Bénard convection for a Prandtl number of 12.3. *J. Fluid Mech.* **758**, 809–830.

WEI, P., CHAN, T.-S., NI, R., ZHAO, X.-Z. & XIA, K.-Q. 2014 Heat transport properties of plates with smooth and rough surfaces in turbulent thermal convection. *J. Fluid Mech.* **740**, 28–46.

WILLERT, C., DU PUITS, R. & RESAGK, C. 2014 Investigation of the turbulent boundary layer in high Rayleigh number convection in air using long PIV sequences. In *17th International Symposium on Applications of Laser Techniques to Fluid Mechanics, Lisbon, Portugal*.

ZHOU, Q. & XIA, K.-Q. 2010 Measured instantaneous viscous boundary layer in turbulent Rayleigh–Bénard convection. *Phys. Rev. Lett.* **104**, 104301.